

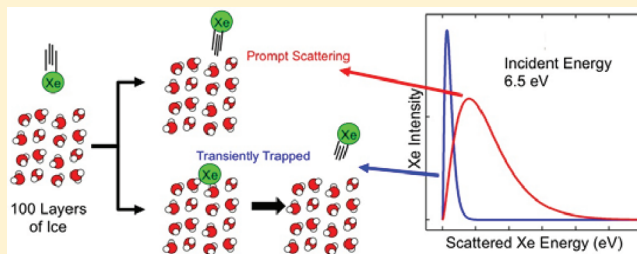
# Scattering of High-Incident-Energy Kr and Xe from Ice: Evidence that a Major Channel Involves Penetration into the Bulk

K. D. Gibson,<sup>†</sup> Daniel R. Killelea,<sup>†,§</sup> Hanqiu Yuan,<sup>†</sup> James S. Becker,<sup>†</sup> Subha Pratihar,<sup>‡</sup> Paranjothy Manikandan,<sup>‡</sup> Swapnil C. Kohale,<sup>‡</sup> W. L. Hase,<sup>‡</sup> and S. J. Sibener\*,<sup>†</sup>

<sup>†</sup>The James Franck Institute and Department of Chemistry, The University of Chicago, 929 East 57th Street, Chicago, Illinois 60637, United States

<sup>‡</sup>Department of Chemistry and Biochemistry, Texas Tech University, Lubbock, Texas 79409, United States

**ABSTRACT:** The scattering of high kinetic energy (1–6.5 eV) xenon and krypton atoms from ice was experimentally measured and theoretically modeled. The ice efficiently accommodates translational energy, but the extent to which the energy is quenched suggests the mechanism for the highest energies and near-normal incidence angles involves more than interaction with just the molecules at the ice surface. Simulations show that for these conditions the xenon penetrates into the selvedge. This penetration into the solid manifests experimentally in that the postcollision translational energy is essentially independent of the incident translational energy. This observation is in stark contrast with what is usually the situation for scattering from a surface. Finally, postexposure desorption measurements showed that some of the incident gas atoms were trapped in the bulk of the ice at temperatures well above where the absorption is thermodynamically stable. The above evidence leads to the conclusion that under conditions of near-normal angles of incidence and high collision energy, much, if not most, of the rare gas penetrates below the ice surface and into the selvedge. A fraction is stably embedded in the near surface region of the ice, whereas the remaining rare gas escapes with two distinct velocity distributions; the first is a result of a thermal process and the second, faster distribution, is the result of ejection from the solid.



## INTRODUCTION

The initial step in many important surface reactions is the adsorption of gas-phase constituents. For the reactant to remain on the surface for sufficient time to facilitate reaction, any excess energy from the collision with the surface must be dissipated away from the nascent collision complex. If the dissipation is facile, the atom or molecule will be able to become trapped in the surface potential well. If the system is unable to stabilize the collision complex, then the gas-phase species will promptly desorb from the surface.

Aside from simply adsorbing to the surface, an atom or molecule can be buried, or *absorbed*, into the bulk of the solid. This may occur via a mechanism where the species is transiently trapped on the surface and becomes buried by the adsorption of more material on the surface, but in the absence of additional condensate, this approach would be ineffective in the trapping of a gaseous species in a solid. A tantalizing approach would be to inject the gas-phase species directly into the solid. Gibson et al.<sup>1</sup> saw evidence that 3.6 eV Xe could penetrate well below the surface of a self-assembled monolayer (SAM). After penetration, the xenon atoms were expelled with energy greater than what would be possible if the xenon had thermalized with the surface. Similarly, Tasić and Troya<sup>2</sup> predicted that hyperthermal Ar impinging on a SAM surface would readily penetrate into the SAM because the kinetic energy of the incident Ar could overcome any penetration

barrier. Furthermore, they calculated that the energy distribution of the Ar escaping from beneath the surface would be independent of the initial energy but not thermalized to the SAM temperature.

Another process that occurs with these high translational energy collisions is the sputtering of the ice surface. However, even at the largest Xe translational energy, the flux of sputtered water is only ~1% of the incident Xe flux. The results of neutral sputtering of water has been discussed in a recent publication.<sup>3</sup>

Scattering experiments in which the energies and angles of both the incident and scattered atoms or molecules are precisely measured yield information about how energy is dissipated into the solid via gas–surface interactions. The use of rare gases simplifies the analysis of these experiments because there are no internal degrees of freedom in the gas and the interaction potentials are well-known and straightforward to model. In the current Article, the scattering of both Xe (experimentally and theoretically) and Kr (experimentally) from ice surfaces as a function of incident translational kinetic energy ( $E_I$ ), incident angle ( $\Theta_I$ ), and scattering angle ( $\Theta_F$ ) was investigated to understand the interaction between the ice and the incident atoms. These results clearly demonstrate that gases

Received: December 16, 2011

Revised: June 3, 2012

Published: June 25, 2012



with sufficient  $E_i$  do not only scatter off the repulsive wall of the gas–surface interaction at the ice surface but also may penetrate into the ice selvedge and even become embedded in the bulk. We will discuss our experiments of translationally energetic Xe and Kr colliding with both crystalline ice (CI) and amorphous solid water (ASW). This was done with Xe and Kr having average incident energies ( $E_i$ ) between 1 and 6.5 eV and as a function of incident angle ( $\Theta_i$ ) and scattering angle ( $\Theta_f$ ).

Andersson et al.<sup>4</sup> measured and theoretically simulated the scattering of Ar from crystalline ice surfaces with an  $E_i$  range between 0.065 and 0.93 eV, and Bolton et al.<sup>5,6</sup> modeled the same system with  $E_i$  between 0.1 and 2.0 eV. They suggested that there were two distinct velocity distributions in the postcollision time-of-flight (TOF) spectra, both attributed to interaction with the ice surface. The slower component was characterized by a Maxwell–Boltzmann distribution with an average final energy ( $\langle E_f \rangle$ ) of  $2k_B T_s$ , where  $k_B$  is Boltzmann's constant and  $T_s$  is the surface temperature. Furthermore, the angular distribution of the slow component was proportional to  $\cos(\Theta_f)$ . These atoms are transiently trapped and thermally equilibrated with the surface before desorbing. This type of scattering is known as trapping-desorption (TD); all memory of the initial energy and angle has been lost. The faster component is due to atoms scattered through a direct inelastic scattering (IS) process from the surface of the ice. The measured  $\langle E_f \rangle$  is dependent on  $\Theta_i$ ,  $\Theta_f$ , and  $E_i$ , with  $\langle E_f \rangle$  increasing as  $E_i$  increases. These are atoms that only interacted briefly with the surface, probably after only encounters with a few ice molecules. One aspect of the Ar–ice interaction detailed by Bolton et al. was how the impact site on the ice can affect the scattering event. Their calculations suggested that when Ar impacted on the open  $I_h$  hexagon the six water molecules collectively expanded to accommodate the Ar atom but then contracted, expelling the Ar.<sup>6</sup> The ice efficiently dissipates the collision energy so that a major fraction of the scattering is the thermalized TD component, and even the IS component has  $\langle E_f \rangle$  much less than  $E_i$ .

There is theoretical modeling for HF<sup>7</sup> and HCl<sup>8</sup> colliding with the (0001) face of ice  $I_h$ . One particular feature is that with sufficient  $E_i$  and at near-normal  $\Theta_i$  the molecules can actually penetrate well below the ice surface. This was attributed to the open structure of the ice crystal. As  $\Theta_i$  becomes more glancing, the molecules no longer penetrate, and the incident molecules scatter from the ice surface. There are also simulations of O(<sup>3</sup>P)<sup>9</sup> and Ar<sup>2</sup> colliding with ordered SAM surfaces grown on a solid substrate. Like ice, the SAM surface can absorb much of the incident energy of the colliding atom, although it is morphologically different in that there are continuous channels between neighboring alkane chains all of the way to the substrate. For near-normal  $\Theta_i$  and  $E_i \gtrsim 3$  eV for O(<sup>3</sup>P) and  $\gtrsim 6$  eV for Ar, many of the colliding atoms penetrate well below the surface of the SAM but can still be scattered with a translational energy greater than expected for thermal accommodation. In particular, for 6–12 eV Ar, the final energy is independent of  $E_i$  and  $\Theta_i$  for  $\Theta_i = 0$  and  $30^\circ$ , with the scattered intensity peaking toward normal. At  $\Theta_i = 60^\circ$ , most of the scattering is from the ice surface and the energy accommodation is less than that for near-normal  $\Theta_i$ .  $E_f$  is dependent on  $E_i$ , increasing as  $E_i$  increases, and the postcollision intensity and  $E_f$  are greater at glancing  $\Theta_f$ .

The experiments described in the present paper used D<sub>2</sub>O ice, at least 1000 layers thick, deposited on a Rh(111) substrate. Careful control over the deposition conditions yielded an ice

that was not a single crystal, which is representative of naturally occurring ice. However, the water molecules will still have some definite arrangement over small distances, with the same open structure, and so comparison with the single-crystal simulations is valid. For Xe with  $E_i$  between 1 and 6.5 eV colliding with a thick ice layer, the postcollision features in the scattering experiments have the same qualitative features as for the Ar–SAM simulations, which we interpret as evidence that much of the Xe penetrates into the bulk at  $\Theta_i$  near normal and interacts primarily with the surface at glancing  $\Theta_i$ . Herein, along with a recent paper,<sup>10</sup> we show that Kr with  $E_i = 3.1$  eV and fast Xe, incident at near-normal  $\Theta_i$ , are absorbed by the ice at temperatures well above where the absorption is thermodynamically stable. These atoms are kinetically trapped in the selvedge region; the rare gas atoms penetrated, and a portion were metastably embedded at defects in the ice structure.

## METHODS

### Simulation Model and Computational Methodology.

Classical chemical dynamics simulations of Xe atom colliding with the basal (0001) plane of a hexagonal ice slab were performed using a modified TIP4P<sup>11</sup> potential for water. The TIP4P model assumes rigid water molecules with no explicit polarizability. To allow energy transfer to the internal degrees of freedom of the water molecules, we included harmonic intramolecular potentials for water with stretching and bending force constants of 8.4 mdyn/Å and 0.70 mdyn·Å/rad<sup>2</sup>, respectively. The unit cell for the ice surface is that of Hayward and Reimers,<sup>12</sup> and a large ice model was used consisting of 10 bilayers with 1600 water molecules (Figure 1). The model was optimized at 0 K and gives a structure in accord with that of ice.

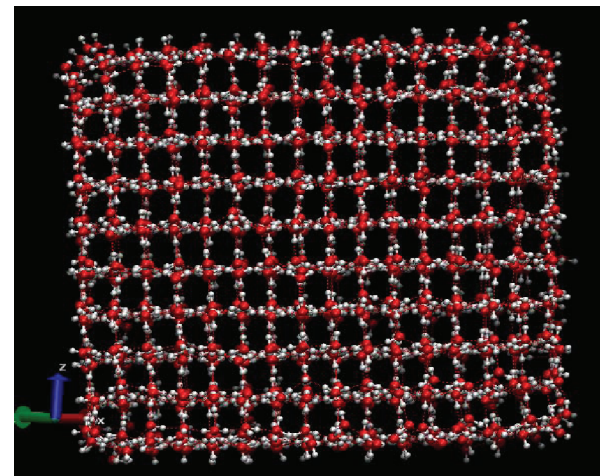


**Figure 1.** Optimized ice ( $I_h$ ) model with 10 bilayers and 1600 water molecules.

The Xe–ice interaction potential was derived by fitting electronic structure calculations performed for Xe interacting with H<sub>2</sub>O and (H<sub>2</sub>O)<sub>2</sub>. The MP2/aug-cc-pVDZ (LANL2DZ for Xe)<sup>13–15</sup> level of theory was used in these calculations with BSSE corrections included. Energies as high as 6.5 eV were included in the calculations to represent the high collision energies of the Xe + ice experiments. The interaction between Xe and the surface O and H atoms is represented by the two-body function

$$V_{xy} = A_{xy} \exp(-B_{xy}r) + \frac{C_{xy}}{r^n} + \frac{D_{xy}}{r^m} \quad (1)$$

where the  $D_{xy}/r^m$  term is added to the Buckingham potential to provide additional flexibility in the fitting. The respective  $A_{xy}$ ,  $B_{xy}$ ,  $C_{xy}$ , and  $D_{xy}$  parameters for Xe–O and Xe–H are provided in Table 1. The resulting Xe/H<sub>2</sub>O and Xe/(H<sub>2</sub>O)<sub>2</sub> analytic interaction potentials are in excellent agreement with the electronic structure calculations.

**Table 1. Parameters for the Xe–H and Xe–O Two-Body Interactions**

	Xe–H	Xe–O
A (kcal/mol)	13611.7	90903.5
B (kcal/mol)	3.25177	3.14436
C (kcal/mol)	−1743.24	−8774.70
D (kcal/mol)	2430.85	0.0001397876
N	7	7
M	9	9

The classical trajectory simulations were performed using the general chemical dynamics program VENUS.<sup>16,17</sup> Initial conditions were chosen to model the experiments. Simulations were performed for Xe translational energies of 3.9, 4.6, 5.7, and 6.5 eV and incident angles of 0 (normal), 25, 45, and 65°. The Xe atoms were directed to impact the ice surface along the *z* axis randomly on a surface area covering the middle unit cell of the model (Figure 2). Initially the top eight bilayers were

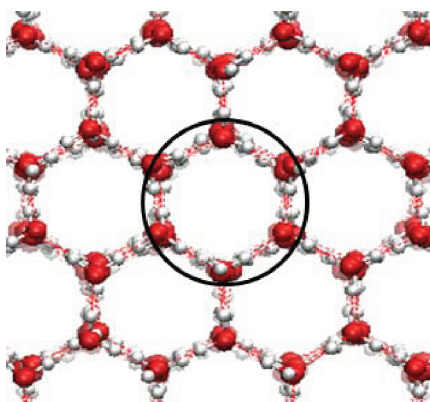


**Figure 2.** Surface area of one unit cell of ice-I<sub>h</sub> along the *z* direction.

thermalized at a temperature of ~140 K and the bottom two bilayers were held fixed during the simulations. The Xe atoms penetrated only as deep as the third bilayer, and tests showed that the results were not changed by using larger models with more bilayers. For productive simulations, the top six bilayers were thermalized, and the bottom four bilayers were held fixed to reduce simulation time. A total of 1600 trajectories were calculated for each collision energy. They were propagated to 6 ps using the Adams–Moulton integration algorithm in VENUS with a time step of 0.2 fs. The trajectories were analyzed to determine the translational energies and scattering angles for the scattered Xe atoms. The latter is defined by the angle between the final velocity vector of Xe and the surface normal. Also determined was the probability that Xe penetrated the surface, the depth of penetration, and the position of Xe in the surface or if it had desorbed when the trajectory was halted.

The model used here for the hyperthermal Xe + ice simulations is similar to those used previously. Bolton and coworkers<sup>4,6</sup> studied Ar + ice collisions at energies of 1 eV and less, much lower than those considered here, and used a much smaller ice model but included periodic boundary conditions (PBCs). To study the scattering of alkali ions from an ice surface, Lahaye<sup>18</sup> used a large ice model, as used here, and also without PBCs. PBCs were not used because of complications that would arise from periodic impact effects on the ice surface at hyperthermal energies.<sup>18</sup> The same consideration was made in developing the model used here. A sufficiently large ice model was used so that there are no boundary effects between the middle unit cell, from which Xe scatters, and the edges of the ice model.

**Experimental Section.** The measurements were done in a UHV scattering chamber (base pressure  $10^{-10}$  Torr) with the capability to produce up to three independent atomic or molecular beams.<sup>19</sup> The beams all converge at the position of a Rh(111) target crystal mounted on a rotatable manipulator, allowing for changing of the incident polar angle,  $\Theta_I$ , of the impinging beam. The temperature of the Rh substrate was regulated with resistive heating and cryogenic cooling using either liquid N<sub>2</sub> or He and was measured with a type K thermocouple welded to the Rh. Postcollision atoms were detected with a precision-aligned rotatable differentially pumped quadrupole mass spectrometer (QMS) allowing for the measurement of the postcollision gas flux at various  $\Theta_F$  with ~1° fwhm resolution. There are physical limits to the  $\Theta_F$  that can be explored depending on the  $\Theta_I$ , the most normal  $\Theta_F = 45^\circ - \Theta_I$  for  $\Theta_I \leq 45^\circ$ . For instance, when  $\Theta_I = 0^\circ$ , the closest  $\Theta_F$  can be to normal is 45°.

All of the ices studied were composed of D<sub>2</sub>O, grown by molecular beam dosing using helium bubbled through a room-temperature reservoir of D<sub>2</sub>O and expanded at stagnation pressures of a few hundred Torr through a 200 μm pinhole. (D<sub>2</sub>O was used in these studies because the detector had a much higher *m/e* 18<sup>+</sup> than *m/e* 20<sup>+</sup> signal, making it much easier to look for sputtered molecules.) Initially, a clean Rh(111) surface was prepared by a combination of Ar<sup>+</sup> sputtering, baking in O<sub>2</sub> at 900 K and annealing at ~1250 K. This surface was then exposed to an O<sub>2</sub> beam at  $T_S = 450$  K for sufficient time to grow an ordered 0.5 monolayer of O on the surface,<sup>20</sup> as evidenced by low-energy He diffraction. This was cooled to ~140 K (for CI) or 115–120 K (for ASW) and then exposed to the D<sub>2</sub>O beam for times sufficient to grow ≥1000 layers on top of the previously prepared O–Rh(111) surface. The O–Rh(111) surface was chosen because it allows accurate and reproducible control over the morphology of the ice and to allow us to compare scattering dynamics from ASW and CI. Ice structures had no long-range order, as determined by 18 meV He scattering, but the Rh(111) surface was completely wetted at ice thicknesses used, verified by CHCl<sub>3</sub> exposure, followed by temperature-programmed desorption (TPD).<sup>21</sup> Under these growth conditions, the ice surface was not porous.<sup>22–24</sup>

The rare gas beams were produced by expanding a mixture of a few percent of either Kr or Xe in He or H<sub>2</sub> at a few hundred PSIG backing pressure through a 20 μm nozzle, held at a temperature between 330 and 650 K. The energy of the incident beam was measured utilizing a precollision mechanical chopper (a rotating slotted disk) and TOF techniques. This was achieved with the Rh(111) sample moved out of the molecular beam path so that the QMS could be rotated to measure the incident beam energy and intensity. Examples of

the beams produced are Xe with an  $E_I = 6.5$  eV (fwhm 6.0 to 6.9 eV) or  $E_I = 1.7$  eV (fwhm 1.6 to 1.8 eV) and Kr with  $E_I = 3.1$  eV (fwhm 2.9 to 3.4 eV). With the elevated nozzle temperatures and dilute gas mixtures, we saw no indication of any clustering in the beam.

The  $\langle E_F \rangle$  of the postcollision atoms was measured using a cross-correlation chopper affixed in front of the entrance aperture of the QMS. Figure 3 shows an example of a

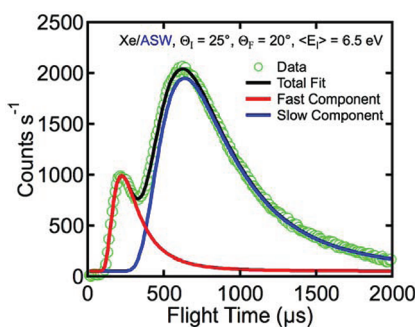


**Figure 3.** Example of a deconvoluted TOF spectrum of Xe scattered from ASW fit with a fast and slow component. The fast component is a shifted Maxwell–Boltzmann velocity distribution, whereas the slow component is a Maxwell–Boltzmann velocity distribution at the surface temperature. The conditions are:  $\Theta_I = 25^\circ$ ,  $\Theta_F = 20^\circ$ , and  $E_I = 6.5$  eV.

deconvoluted TOF spectrum. The data (green circles) were fit with two velocity distributions, a fast component (red line) and a slow component (blue line). As would be expected for atoms desorbing from the surface after thermalizing, the slow component was well-described by a single Maxwell–Boltzmann velocity distribution with a characteristic temperature equal to that of the surface

$$f(v) \propto v^3 \exp\left(\frac{-mv^2}{2k_B T_S}\right) \quad (2)$$

The fast velocity distribution was fit to a shifted Maxwell–Boltzmann distribution, with both  $v_0$  and  $T$  as adjustable parameters

$$f(v) \propto v^3 \exp\left(\frac{-m(v - v_0)^2}{2k_B T}\right) \quad (3)$$

Molecules which were trapped on the surface or even transiently adsorbed had significant residence times. The use of the post-target chopper allowed us to accurately measure the velocity after the molecules left the surface. It is also important to note that all of the spectra were taken in a plane defined by the incident beam and the arc of the detector rotation, with the target crystal surface perpendicular to this plane. For any ice we grew, several spectra at different  $\Theta_F$  (but the same  $\Theta_I$ ) were taken before the ice was desorbed and a new ice grown. The first and last spectra were for the same conditions. This allowed us to monitor whether there were any collision-induced changes in the ice surface that affected the results. Except  $\Theta_I = 65^\circ$ , the before and after spectra were the same within our experimental error.

The  $D_2O$  coverage was determined by TPD, where the signal of desorbing  $D_2O$  was measured with the QMS while the target temperature was ramped. The absolute amount was referenced to one full layer of  $D_2O$ , grown under conditions where only

the layer nearest the clean Rh(111) surface sticks. He diffraction was consistent with a  $(\sqrt{3} \times \sqrt{3})R30^\circ$  structure, with a coverage of 0.67  $D_2O$  molecules per Rh atom on the Rh(111) surface.<sup>25</sup> As mentioned, the growth temperature determined whether the deposited ice film was ASW or CI. This could be confirmed by the TPD spectra where the leading edge (low temperature side) is considerably different for the two forms of ice.<sup>26</sup>

To determine Xe coverage, a monolayer of xenon was grown on the Rh(111), similar to what was done for Ag(111).<sup>27</sup> The clean Rh(111) was exposed to a low-pressure ( $\sim 100$  Torr) room temperature beam of pure Xe expanded through a 200  $\mu\text{m}$  nozzle. The surface temperature was adjusted so that only a single layer was adsorbed, and the sticking coefficient was assumed to be unity until the coverage was complete. This assumption was validated by monitoring the Xe signal with a residual gas analyzer (RGA) that was positioned out of the beam path so that only the background gas was measured. The entire beam was intercepted by the cold Rh crystal, and when it was exposed, the Xe RGA signal changed little until the surface was completely covered. The integrated TPD signal was used to calibrate the QMS signal for one layer. The time taken to reach monolayer coverage gave an absolute measure of the flux of a room-temperature pure Xe beam. The Xe RGA signal from any of the seeded Xe beams made could then be referenced to that of the room-temperature pure Xe beam to determine the flux of the seeded beam. Kr exposure was estimated with reference to the Xe signal. A comparison of the UHV chamber ion gauge pressure increase for a pure Xe beam and a pure Kr beam, after correcting for the relative ionization probabilities, was used to calibrate the RGA for the Kr flux. A Kr beam with a known flux and the different lattice constants of a Xe and Kr monolayer were then used to calibrate the QMS for a layer of Kr.

## RESULTS AND DISCUSSION

**Simulations.** Simulations for high-energy Xe colliding with the ice  $I_h$  surface indicate that much of the Xe penetrates below the ice surface. The probability of reaching a certain depth beneath the ice surface as a function of  $\Theta_I$  and  $E_I$  is shown by the center three panels in Figure 4. For  $\Theta_I$  of 0 and  $25^\circ$ , all of the trajectories penetrate below the ice surface for collision energies between 3.9 and 5.7 eV. Nonpenetrating trajectories are present for  $\Theta_I = 45^\circ$ , 15% of the total at 3.9 eV. The near surface of the ice is divided into four regions: the region of the first water bilayer, the region between the first and second bilayers, the region of the second bilayer, and the region between the second bilayer and third bilayer, shown schematically at the top of the Figure. At  $\Theta_I = 45^\circ$ , much of the Xe does not get much below the first water layer regardless of the incident translational energy. As  $\Theta_I$  becomes smaller, the xenon penetration is often deeper, with much of the Xe with collision energies of 5.71 eV incident at  $\Theta_I = 0^\circ$  penetrating below the second water layer. The bottom panel of the Figure shows the average penetration depth for the various incident ensembles. Clearly, penetration of the ice is highly probable, and the simulation results suggest that most Xe atoms are injected at least beneath the surface layer of the ice.

The probability that Xe atoms remain trapped within the ice when the simulation is halted after 6 ps have elapsed is shown in the bottom panel of Figure 4. The probability increases with increasing collision energy and decreasing incident angle, with the lowest fraction at  $\Theta_I = 45^\circ$  and  $E_I = 3.88$  eV (16% of the total) and the highest fraction at  $\Theta_I = 0^\circ$  and  $E_I = 5.71$  eV (61%

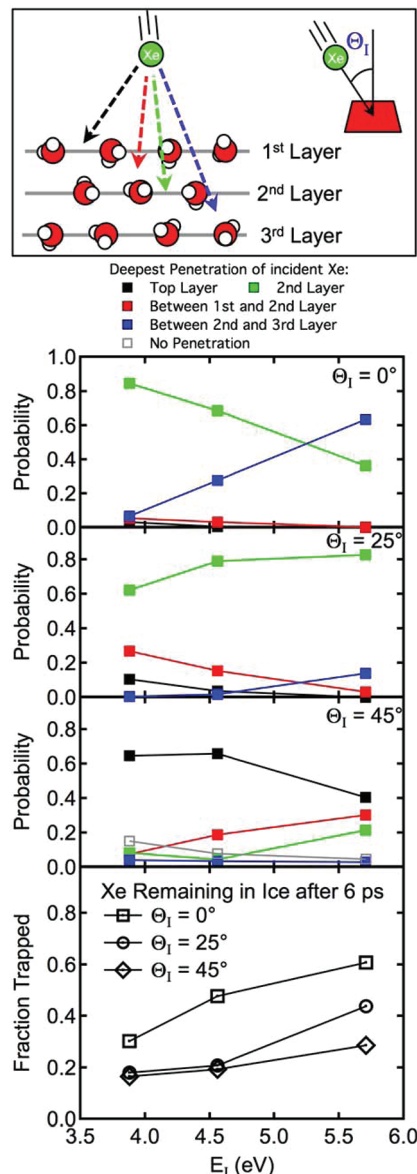


**Figure 4.** Penetration of the (0001)  $I_h$  surface, at 140 K, found from classical trajectory chemical dynamics simulations for  $E_i = 3.9, 4.6$ , and  $5.7 \text{ eV}$  and  $\Theta_i$  of  $0^\circ, 25^\circ$ , and  $45^\circ$ . The cartoon at the top shows the different calculated penetration depths in terms of layers of water molecules near the ice surface ( $z$  direction). The three panels show the probability for incident Xe atoms reaching some depth. Xe was calculated to always penetrate, except at glancing incidence,  $45^\circ$ , where a small fraction (15% at 3.9 eV, 4.5% at 5.7 eV) scatters off the surface (gray open squares). The lowermost panel shows the probability that the Xe atoms are trapped within the ice when the simulations are halted after 6 ps.

of the total). The Xe rapidly equilibrates with the ice, but the thermal equilibration is not complete at 6 ps. At 140 K, an equilibrated Xe atom would have an energy of 18 meV, but the average energy of the Xe atoms still within the ice was 24–28 meV for  $\Theta_i$  of  $0^\circ$  or  $25^\circ$  and 45–83 meV at  $\Theta_i = 45^\circ$ .

Bolton et al.<sup>5,6</sup> simulated the collision of Ar ( $E_i$  between 0.1 and 2.0 eV) colliding with hexagonal ice having surface temperatures between 0 and 180 K. They found very efficient and rapid energy exchange between the Ar and ice, with much of the Ar becoming trapped on the surface. Any penetration was only past the first layer of the ice structure, and much of the

penetration happened after trapping on the surface. This was facilitated at the higher temperature (180 K), where the surface structure was becoming very distorted by the thermal motion of the molecules.

**Experiment. Near-Normal Incident Angles.** The left-hand panels in Figure 5 show examples of the integrated intensity (top) and average final energy (bottom) for Xe with  $E_i = 6.5 \text{ eV}$  scattering from CI or ASW at  $T_s = 120 \text{ K}$  and  $\Theta_i = 0^\circ$ . The intensity ( $y$  axis) scales are the same, so the results can be directly compared. For the slow data plotted in the intensity curves, the solid line is a least-squares fit proportional to  $\cos(\Theta_F)$ , and the data are well-fit with a Maxwell–Boltzmann velocity distribution with  $\langle E_F \rangle = 2kT_s$ . These two observations are indicative of a TD channel. Unlike the scattering of 0.4 eV Ar,<sup>28</sup> we did not observe a significant difference between the scattering of the high-energy Xe from CI and ASW. Therefore, the right-hand-side two panels of Figure 5 show the average of all of the experiments done on both CI and ASW.

Figure 6 shows the translational energy of the fast component of the angle-resolved scattering of Xe from CI and ASW at  $\Theta_i = 25^\circ$  for different incident energies. All of the ASW data and most of the CI data were taken at  $T_s = 115\text{--}118 \text{ K}$ , and some of the CI data were taken at  $T_s = 140 \text{ K}$ . Although not shown, the intensities show a regular progression, with the amount of the in-plane fast component increasing and the TD component decreasing as the incident translational energy is decreased.

We want to focus on the energy of the fast component. For the conditions shown in Figure 5,  $\Theta_i = 0^\circ$  and  $E_i = 6.5 \text{ eV}$ , 98 to 99% of the incident energy is lost to the ice, even for the Xe that was not thermally accommodated (fast channel). At  $\Theta_i = 25^\circ$ , the data in Figure 6, the energy loss for the fast component is slightly lower, and the angular dependence changes, with the slightly faster Xe at more glancing final angles. For both  $\Theta_i$ , most of the incident energy is exchanged with the ice surface, as previously reported for Ar with  $E_i \lesssim 1 \text{ eV}$ .<sup>4,28</sup> However, for the Xe data at  $\Theta_i = 25^\circ$ , the energy of the fast component is almost independent of  $E_i$  between  $\sim 1$  and  $6.5 \text{ eV}$ . At the simplest approximation, Baule theory<sup>29</sup> predicts that for scattering from the surface of the ice  $\Delta E \propto E_i$ , but  $E_F$  is nearly identical even though  $E_i$  has changed by a factor of  $\sim 6$ . (This comparison is a little suspect because the Xe is almost six times heavier than the D<sub>2</sub>O, making the probability of a single impact unlikely.) Experimentally, many systems show a direct correlation between the  $E_i$  and  $E_F$ . Some examples are Ar from Ag(111),<sup>30</sup> Ar from SAMs,<sup>31</sup> and Ar from ice,<sup>4</sup> all attributable to scattering from the surface. However, for high incident energies and near-normal incident angles, HF,<sup>7</sup> HCl,<sup>8</sup> and Xe<sup>32</sup> are predicted to penetrate easily below the surface of ice  $I_h$  due to its open structure. Gibson et al.<sup>1</sup> saw evidence that 3.6 eV Xe could penetrate well below the surface of a SAM and be expelled with an energy much higher than that expected for thermalization to the surface temperature. Similarly, Tasić and Troya<sup>2</sup> predict that hyperthermal Ar impinging on a SAM surface can easily penetrate, and the Ar escaping from below the surface has an energy distribution independent of the initial energy but is not thermalized to the SAM temperature. In addition, simulations show that there is deep penetration of a 1-decanethiol SAM by hyperthermal, near-perpendicular collisions of O(<sup>3</sup>P) atoms, with efficient energy transfer.<sup>9</sup>

As noted, the  $\langle E_F \rangle$  distributions are different at  $\Theta_i = 0^\circ$  and  $25^\circ$ , having a slightly greater value, which peaks at more glancing  $\Theta_F$  for  $\Theta_i = 25^\circ$ . One possibility is that as  $\Theta_i$  becomes

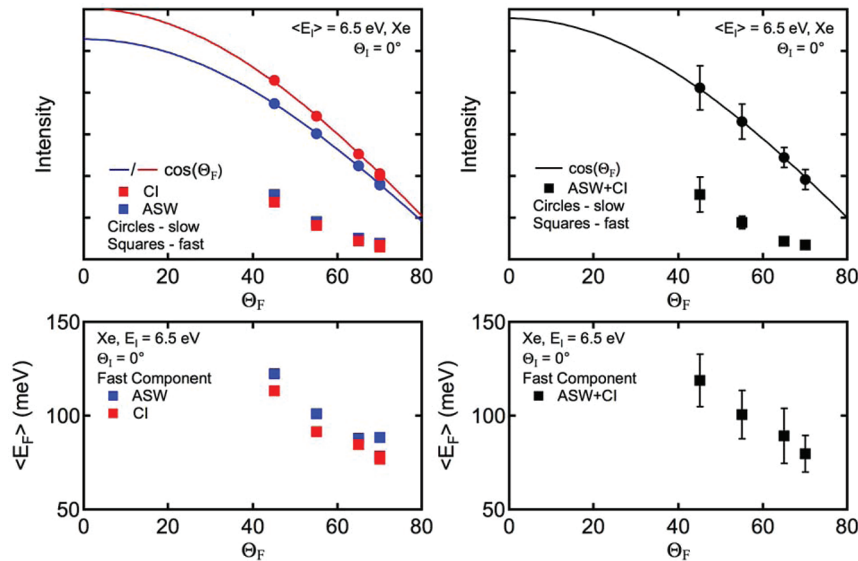


**Figure 5.** Left two panels show the intensities of the fast and slow components (top panel) and the average translational energies of the fast components (lower panel) for Xe scattering from CI (red) and ASW (blue) with an  $E_I = 6.5$  eV and  $\Theta_I = 0^\circ$ . The right-hand panels show the average of all data taken with these incident conditions for both CI and ASW. The intensity axes are in arbitrary units but have the same scale.

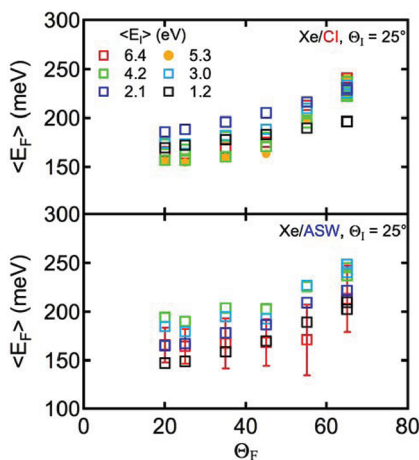


**Figure 6.** Average energies of the fast component for Xe scattered from CI and ASW at different incident energies and  $\Theta_I = 25^\circ$ . As with all of the Figures, multiple points for the same conditions are from replicate experiments to highlight the reproducibility.

more glancing, more of the Xe is scattered from the surface, and this Xe retains more of its initial energy, as suggested for HF,<sup>7</sup> HCl,<sup>8</sup> and Ar from SAMs.<sup>2</sup> This will be discussed later with the results of experiments done at glancing  $\Theta_I$ .

Figures 7 and 8 show some results for Kr scattered from CI and ASW at  $\Theta_I = 0$  and  $25^\circ$ , respectively. As with the Xe, almost all of the energy is transferred to the ice, and the energy of the Kr scattered via the fast channel is virtually the same from both ASW and CI (Figure 7, lower) at  $E_I = 3$  eV. Figure 8 shows  $\langle E_F \rangle$  for Kr with  $E_I = 3.1$  and  $0.7$  eV. At the more glancing incidence ( $\Theta_I = 25^\circ$ ),  $\langle E_F \rangle$  is slightly greater at normal incidence. Also, as incidence moves away from normal, the trend for decreasing  $\langle E_F \rangle$  with increasing  $\Theta_F$  shifts. At  $\Theta_I = 25^\circ$ , as shown in Figure 8,  $\langle E_F \rangle$  increases with increasing  $\Theta_F$ . Figure 8 also shows results for  $E_I = 0.7$  eV. It is interesting to see that the fast scattering for both xenon and krypton are qualitatively similar; there is little dependence of the final

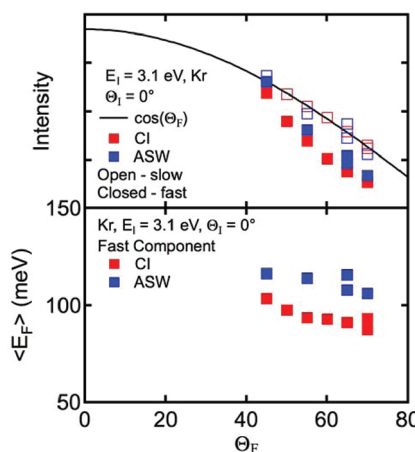


**Figure 7.** Angular distributions of the intensities (top) and average energies of the fast component (lower) for Kr with  $E_I = 3.1$  eV scattered from CI (red) and ASW (blue) at  $\Theta_I = 0^\circ$ . The intensity axes are in arbitrary units but have the same scale.

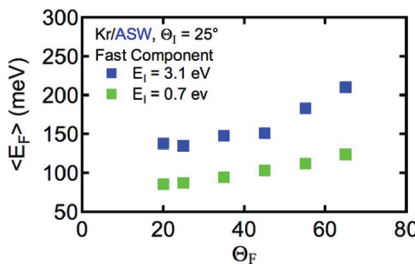


**Figure 8.** Average energies of the fast component for Kr with  $E_I = 3.1$  (blue) and  $0.7$  eV (green) scattered from ASW at  $\Theta_I = 25^\circ$ .

energy on the incident energy, and both the TD and fast channels are observed.

So far, we have shown the results of simulations that indicate that high-energy projectiles can penetrate below the first ice layer. We also presented indirect evidence of the penetration, the independence of the scattered energy from the collision

energy. In systems with lower collision energies and/or more glancing incident angles, there is normally a direct correlation between the energy in and out. As outlined in the previous paragraphs, one possibility for the final energy independence is that some, if not most, of the atoms penetrate and interact with water molecules in the selvedge for a sufficient time that the initial conditions no longer matter.

To gather direct evidence that some of the impinging rare gas had penetrated, we examined the rare gas signal while concurrently measuring the D<sub>2</sub>O TPD signal during post-collision desorption measurements. When an ice surface was cooled using liquid He as the cryogen, it was possible to absorb Xe to the ice surface using a low-energy beam of Xe ( $E_I \approx 63$  meV). A TPD spectra for this surface showed the Xe desorbing at ~70 K, which is the desorption temperature for Xe adsorbed on other surfaces, for instance Ag(111).<sup>33</sup> In a separate paper, we showed that when the ice was exposed to high-energy Xe and at near-normal incident angles, there was a Xe desorption peak above 120 K.<sup>10</sup> This Article also showed evidence that the uptake rate was greater for higher  $E_I$  and more normal  $\Theta_I$ . As previously mentioned, these should be the conditions that lead to a greater probability of subsurface penetration of the impinging atoms. The most likely explanation is that a fraction of the Xe penetrated below the first ice layer and became trapped in the selvedge. We observed a similar phenomenon for exposure of ice to a beam of Kr atoms. Post-collision TPD spectra after exposure of ASW to a Kr beam with  $\Theta_I = 0^\circ$  and  $E_I = 3.1$  eV for various exposures are shown in Figure 9; it is clear

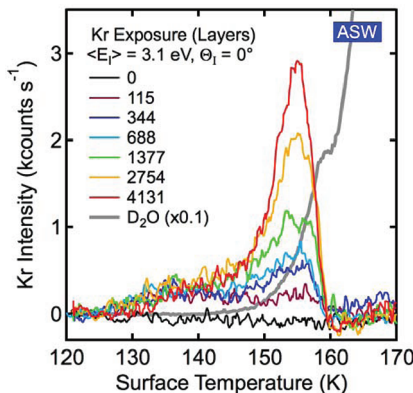


**Figure 9.** Embedding of Kr in ASW. Kr TPD spectra (heating rate = 10 K/min) taken after different exposures of ASW to Kr with  $E_I = 3.1$  eV and  $\Theta_I = 0^\circ$ . The Kr exposures are in layers of Kr, as discussed in the text.

from the TPD that Kr is desorbing well above the surface desorption temperature and well before any appreciable desorption of the ice itself. The desorption temperatures are much higher than would be expected for adsorbed Kr because it should have even a shallower adsorption well than Xe.

Figure 10 shows the uptake of Kr and Xe under various conditions as a function of total exposure at  $T_S = 120$  K. The uptake rate is greatest at the start of the exposure, but the uptake apparently reaches a plateau equivalent to ~1 layer of rare gas, even when the total exposure would have deposited several thousand layers if all of the gas had been trapped in the ice. The ice surfaces showed no long-range order when using low-energy He scattering and so is probably composed of many small crystallites (for CI) or small ASW regions randomly ordered with respect to each other. Therefore, we are unable to

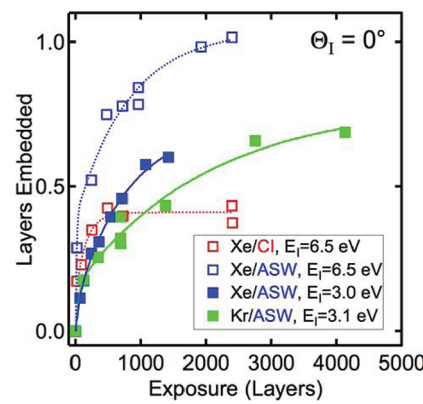


**Figure 10.** Layers of rare gas embedded versus exposure for the listed conditions at  $\Theta_I = 0^\circ$ . The lines are to guide the eye.

say whether the atoms are trapped at interstitial defects rather than in the crystallites themselves.

*Glancing Incident Angles.* Figure 11 shows results for Xe with  $E_I = 6.5$  eV and  $\Theta_I$  between 35 and 65°. As with the

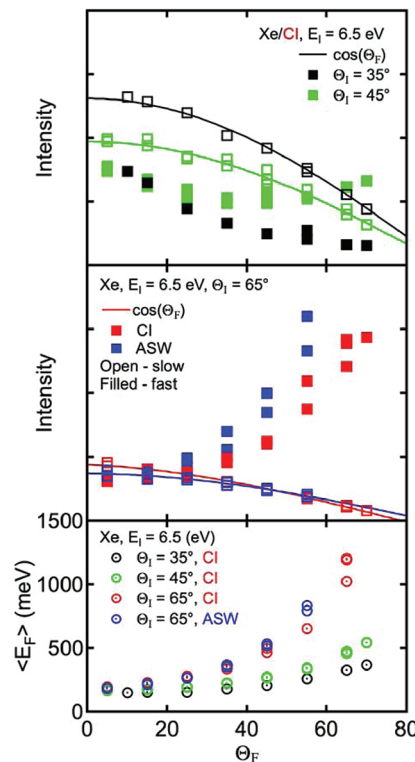


**Figure 11.** Angular distributions of the intensities of the fast (filled squares) and slow (open squares) components of Xe scattered from ice surfaces with  $E_I = 6.5$  eV. The top panel shows the intensity of Xe scattered from CI at  $\Theta_I = 35$  and 45°. The middle panel shows the intensity of Xe scattered from either CI (red) or ASW (blue) at glancing incidence ( $\Theta_I = 65^\circ$ ). The intensity axes are in arbitrary units but have the same scale.

previous Figures, the intensity  $y$  axes are plotted on the same scale so that they are directly comparable. For the slow component, which had an  $\langle E_F \rangle = 2kT_S$ , the solid line is a fit proportional to  $\cos(\Theta_F)$ , except at  $\Theta_I = 65^\circ$ , where it is proportional to  $\cos(\Theta_F - \delta)$ , where  $\delta$  varied from ~4 to 12°. For a  $\Theta_I$  of 35 or 45°, the slow-scattering channel results look like scattering through a TD mechanism, whereas at  $\Theta_I = 65^\circ$ ,

the results appear to be due to trapping—desorption but with a shifted angular intensity distribution. One possible origin of this minor shift is modification of the surface by the high-energy collisions. There are some regular changes in the in-plane scattering results. The ratio of fast to slow intensities increases with increasing  $\Theta_b$ , particularly at larger  $\Theta_F$ , and the energy exchange with the ice decreases with increasing  $\Theta_b$ , particularly at larger  $\Theta_F$ .

Figure 12 shows examples of the how  $\langle E_F \rangle$  changes with varying  $\langle E_i \rangle$  when  $\Theta_I = 65^\circ$  for lower collision energies. These

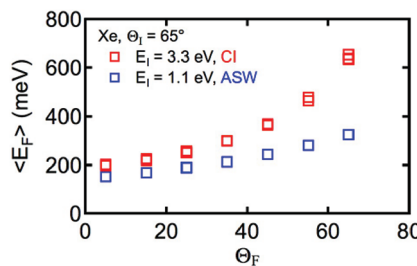


**Figure 12.** Final energies of the fast component for lower incident energy Xe at  $\Theta_I = 65^\circ$ .

results are shown as an example of the final energy increasing with collision energy, an attribute often attributed to scattering from the surface.

As previously mentioned, small molecules can penetrate the rather open ice structure<sup>7,8,32</sup> at near-normal  $\Theta_b$ , and although these calculations were for ordered (0001) ice crystals, the density<sup>22</sup> of ASW is similar to CI and a very open structure.<sup>34</sup> Therefore, exposures involving either CI or ASW will lead to qualitatively similar results. Calculations have been done for  $E_i = 6\text{--}12$  eV Ar colliding with an ordered fluorinated SAM<sup>2</sup> and high translational energy (3.1 and 5.2 eV) O(<sup>3</sup>P) colliding with an ordered 1-decanethiol SAM.<sup>9</sup> Both of these surfaces have large lattice constants (5 Å for the 1-decanethiol and 5.8 Å for the fluorinated SAM) that lead to open surface structures, although they differ from bulk ice in having continuous channels, the space between the parallel C chains. For near-normal  $\Theta_b$ , many of the atoms penetrate beneath the surface, and most of the incident energy is exchanged with the surface. For the Ar collisions,  $E_F$  is independent of  $E_i$ .<sup>2</sup> The angular intensity distribution of the Ar leaving the surface is peaked toward normal. At glancing  $\Theta_b$ ,  $E_F$  increases, particularly at the more glancing  $\Theta_F$ , and the angular intensity distribution also peaks toward glancing  $\Theta_F$ .  $E_F$  becomes dependent on  $E_i$ . The results are qualitatively analogous to what we observe experimentally for the heavier rare gases colliding with ASW and CI.

**Comparison between Experiment and Simulation.** The model for the simulations was a perfect (0001) crystalline ice surface. In contrast, the experimental surfaces consisted of small, imperfect crystallites with interstitial boundaries between domains. However, even with this difference the experiments and simulations have qualitatively similar energy-transfer dynamics. Simulation values of the Xe final energy as a function of  $\Theta_F$  are shown in Figure 13 for a  $\Theta_I$  of 25 and 65°. For  $\Theta_I = 65^\circ$ , the experimental and simulation results are in quite good agreement. The simulation shows that only 35% of the incident trajectories penetrate the surface, with 27% remaining trapped when the trajectories are terminated after 6 ps. The best agreement between experiment and simulation is

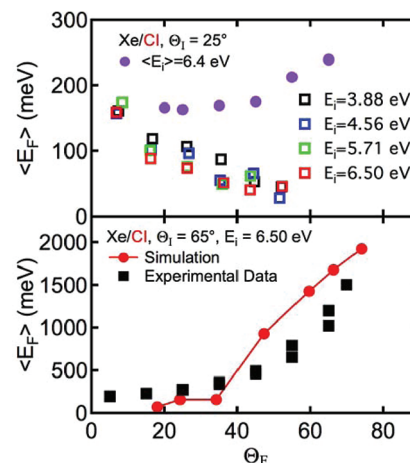


**Figure 13.** Top panel shows  $\langle E_F \rangle$  as a function of  $\Theta_F$  for  $\Theta_I = 25^\circ$  and various Xe collision energies, as determined by the simulations. Included are experimental data for  $\langle E_i \geq 6.4$  eV from Figure 6 (solid circles). The bottom panel compares the angular dependence of the translational energy of the scattered Xe for both experiment and simulation with  $E_i = 6.5$  eV and  $\Theta_I = 65^\circ$ .

for trajectories where direct scattering dominates over penetration.

At  $\Theta_I = 25^\circ$ , experiment and theory have similar final energies, with nearly all of the collision energy adsorbed by the ice. Also, like the experimental results, the simulations show no apparent dependence of  $E_F$  on  $E_i$ . The dependence of the final energy is somewhat different, with the simulation slope more like that of the experimental results at  $\Theta_I = 0^\circ$  (see Figure 5) and no scattering for  $\Theta_F > 50^\circ$ . The differences between experiment and simulation may be due to differences between the surfaces. The narrow angular range over which the Xe escapes in the simulations is consistent with the Xe atoms exiting the bulk along a direction dictated by the perfect crystalline structure. The decrease in  $\langle E_F \rangle$  with increasing  $\Theta_F$  may signify that Xe atoms that undergo more collisions within the channels of the open crystalline ice structure gradually lose more of their energy and may exit at a larger  $\Theta_F$ . The broader angular range seen in the experiments is consistent with a much more disordered ice structure. With increasing  $\Theta_I$  and more glancing collisions, both the experiments and simulations show that the scattered Xe atoms lose less of their initial translational energy.

## CONCLUSIONS

In this Article, we presented the results of experiments and simulations for Xe ( $E_i$  from 1 to 6.5 eV) and Kr ( $E_i$  from 1 to 3.1 eV) colliding with a thick ( $\geq 1000$  layers) D<sub>2</sub>O ice (either CI or ASW). We were able to make double-differential measurements of the postcollision atoms, where both  $\langle E_F \rangle$  and  $\Theta_F$  could be determined as a function of  $E_i$  and  $\Theta_I$ . The TOF spectra can be decomposed into two components, one with a velocity distribution and variation of intensity with  $\Theta_F$  indicative of TD and one that has a higher velocity where the atoms have not thermalized to the ice temperature. The ice is very good at dissipating the collision energy, well over 95% at near-normal  $\Theta_b$ , with most of the postcollision atoms having undergone TD.

Much of the scattering data is for ASW, and some is for CI. Even the CI is at best small crystallites, and there is no 18 meV He specular reflection, which attests to a very disordered

surface. It is smooth enough on the macroscopic scale that for  $\Theta_I \leq 45^\circ$  the slow component had an average energy indicating thermalization with the ice and desorbs with an intensity proportional to  $\cos(\Theta_F)$ , unlike the very rough surface of Suter et al.<sup>28</sup> There is the possibility of surface damage during the course of the exposure. The postcollision velocity measurements did not show changes over time, at least for  $\Theta_I < 65^\circ$ . However, postexposure TPD spectra showed that some rare gas was absorbed, the uptake being very fast upon initial exposure. The location of the rare gas in the ice is unknown: it may create defects or be absorbed at already existing defects. The presence of the adsorbed atoms certainly suggests that the near-surface region of the ice is modified during the course of the experiments.

The fact that the precise nature of the ice surface is unknown, though probably similar to naturally occurring ice, makes precise theoretical modeling difficult. However, a qualitative comparison of the experimental results and the theoretical modeling of a single ice crystal can yield insights into the nature of the rare gas–ice interaction at high collision energies.

The most significant outcome of this study is that for high collision energies and near-normal incident angles, rare gas atoms can penetrate below the surface of the ice and into the selvedge:

- (1) Simulations show that Xe can penetrate as far as the region between the second and third layers of crystalline ice. The penetration decreases with decreasing collision energy and increasing  $\Theta_I$ .
- (2) The TOF distributions of the postcollision atoms have a fast component whose average velocity is experimentally independent of the collision energy. This is not the usual observation for scattering from a surface. In other systems, there is evidence that atoms that have penetrated below the surface can be expelled at energies above thermal. One possibility for the rare gas–ice system is that most of the rare gas penetrates and loses all of its initial energy through collisions with molecules in the selvedge. Some of these rare gas atoms are expelled when the lattice reforms from the distortions, caused by the collision and the presence of a buried atom, and if they have sufficient energy, then they can escape the surface with energy greater than thermal. Therefore, there is no dependence on the collision energy.
- (3) In the postexposure TPD spectra, there is a rare gas signal at temperatures much higher than for surface adsorbed species, suggesting that at least some of the atoms have penetrated and become trapped below the surface of the ice.

As  $\Theta_I$  becomes more glancing, much of the postcollision atoms have been trapped-desorbed, but the fast component of the scattering appears to be more from the surface, with  $\langle E_F \rangle$  of the fast component increasing with  $E_I$  and with an  $\langle E_F \rangle$  and intensity that peaks at glancing  $\Theta_F$ . The simulations bear out this conclusion, as surface scattering predominates at glancing angles and the trends in the final Xe energies as a function of  $\Theta_I$  are the same. The combination of experimental measurements and computer simulations greatly clarifies the study of this system. These results clearly show that scattering of xenon and krypton from ice surfaces is a complex process where the gases penetrate into the selvedge region of the solid and scatter off atoms in the selvedge or even become incorporated into the bulk of the solid.

## AUTHOR INFORMATION

### Corresponding Author

\*E-mail: s-sibener@uchicago.edu.

### Present Address

<sup>§</sup>Department of Chemistry, Loyola University Chicago, Chicago, Illinois.

### Notes

The authors declare no competing financial interest.

## ACKNOWLEDGMENTS

This work was supported by the National Science Foundation CCI Center for Energetic Non-Equilibrium Chemistry at Interfaces (CENECI), Grant No. 0943639, the Air Force Office of Scientific Research and DTRA, Grant. No. HDTRA1-11-1-0001.

## REFERENCES

- (1) Gibson, K. D.; Isa, N.; Sibener, S. *J. Phys. Chem. A* **2006**, *110*, 1469.
- (2) Tasić, U.; Troya, D. *Phys. Chem. Chem. Phys.* **2008**, *10*, 5776.
- (3) Killelea, D. R.; Gibson, K. D.; Yuan, H. Q.; Becker, J. S.; Sibener, S. *J. Chem. Phys. C* **2012**, *136*, 144705.
- (4) Andersson, P. U.; Nagard, M. B.; Bolton, K.; Svanberg, M.; Pettersson, J. B. C. *J. Phys. Chem. A* **2000**, *104*, 2681.
- (5) Bolton, K.; Pettersson, J. B. C. *Chem. Phys. Lett.* **1999**, *312*, 71.
- (6) Bolton, K.; Svanberg, M.; Pettersson, J. B. C. *J. Chem. Phys.* **1999**, *110*, 5380.
- (7) Niel Gardner, D. O.; Al-Halabi, A.; Kroes, G. J. *J. Chem. Phys.* **2004**, *120*, 11796.
- (8) Al-Halabi, A.; Kleyn, A. W.; Kroes, G. J. *J. Chem. Phys.* **2001**, *115*, 482.
- (9) Tasić, U. S.; Yan, T. Y.; Hase, W. L. *J. Phys. Chem. B* **2006**, *110*, 11863.
- (10) Gibson, K. D.; Killelea, D. R.; Becker, J. S.; Yuan, H.; Sibener, S. *J. Chem. Phys. Lett.* **2012**, *531*, 18.
- (11) Jorgensen, W. L.; Chandrasekhar, J.; Madura, J. D.; Impey, R. W.; Klein, M. L. *J. Chem. Phys.* **1983**, *79*, 926.
- (12) Hayward, J. A.; Reimers, J. R. *J. Chem. Phys.* **1997**, *106*, 1518.
- (13) Hay, P. J.; Wadt, W. R. *J. Chem. Phys.* **1985**, *82*, 270.
- (14) Wadt, W. R.; Hay, P. J. *J. Chem. Phys.* **1985**, *82*, 284.
- (15) Hay, P. J.; Wadt, W. R. *J. Chem. Phys.* **1985**, *82*, 299.
- (16) Hase, W. L.; Duchovic, R. J.; Hu, X.; Ormonicki, A.; Lim, K. F.; Lu, D. H.; Peslherbe, G. H.; Swamy, N. K.; Vende Linde, S. R.; Varandos, A. J. C.; Wang, H.; Wolfe, R. J. *QCPE* **1996**, *16*, 671.
- (17) Hu, X.; Hase, W. L.; Pirraglia, T. *J. Comput. Chem.* **1991**, *12*, 1014.
- (18) Lahaye, R. *Surf. Sci.* **2010**, *604*, 1135.
- (19) Gibson, K. D.; Killelea, D. R.; Yuan, H.; Becker, J. S.; Sibener, S. *J. Chem. Phys.* **2011**, *134*, 034703.
- (20) Schwegmann, S.; Over, H. *Surf. Sci.* **1997**, *393*, 179.
- (21) Zimbitas, G.; Hodgson, A. *Chem. Phys. Lett.* **2006**, *417*, 1.
- (22) Brown, D. E.; George, S. M.; Huang, C.; Wong, E. K. L.; Rider, K. B.; Smith, R. S.; Kay, B. D. *J. Phys. Chem.* **1996**, *100*, 4988.
- (23) Stevenson, K. P.; Kimmel, G. A.; Dohnálek, Z.; Smith, R. S.; Kay, B. D. *Science* **1999**, *283*, 1505.
- (24) Kimmel, G. A.; Dohnálek, Z.; Stevenson, K. P.; Smith, R. S.; Kay, B. D. *J. Chem. Phys.* **2001**, *114*, 5295.
- (25) Thiel, P. A.; Madey, T. E. *Surf. Sci. Rep.* **1987**, *7*, 211.
- (26) Speedy, R. J.; Debenedetti, P. G.; Smith, R. S.; Huang, C.; Kay, B. D. *J. Chem. Phys.* **1996**, *105*, 240.
- (27) Gibson, K. D.; Cerjan, C.; Light, J. C.; Sibener, S. *J. Chem. Phys.* **1988**, *88*, 7911.
- (28) Suter, M. T.; Bolton, K.; Andersson, P. U.; Pettersson, J. B. C. *Chem. Phys.* **2006**, *326*, 281.
- (29) Harris, J. Mechanical Energy Transfer in Particle-Surface Collisions. In *Dynamics of Gas-Surface Interactions*; Rettner, C. T.,

Ashfold, M. N. R., Eds.; The Royal Society of Chemistry: Cambridge, U.K., 1991.

(30) Spruit, M.; Vandenhoek, P.; Kuipers, E.; Geuzebroek, F.; Kleyn, A. *Surf. Sci.* **1989**, *214*, 591.

(31) Gibson, K. D.; Isa, N.; Sibener, S. J. *J. Chem. Phys.* **2003**, *119*, 13083.

(32) Pratihar, S.; Kohale, S.; Yang, L.; Manikandan, P.; Hase, W. L., in preparation.

(33) Gibson, K. D.; Sibener, S. J. *J. Chem. Phys.* **1988**, *88*, 7893.

(34) Chowdhury, M. R.; Dore, J. C.; Wenzel, J. T. *J. Non-Cryst. Solids* **1982**, *53*, 247.